Preprint version of the Accepted Author Manuscript (AAM) for the pubblication on the journal: **Philosophical Transactions A** and titled: **Effects of interfacial debonding on the stability of finitely strained periodic microstructured elastic composites**. DOI: 10.1098/rsta.2023.0356

Effects of interfacial debonding on the stability of finitely strained periodic microstructured elastic composites

Fabrizio Greco*[1], Raimondo Luciano[2], Andrea Pranno[1]

[1] *Department of Civil Engineering, University of Calabria, Rende (CS), Italy*
[2] *Engineering Department, University of Napoli Parthenope, Napoli (NA), Italy*

Keywords: highly deformable layered composites, nonlinear homogenization, large deformation contact mechanics, instability, nonlinear cohesive model

---

Abstract

Predicting failure initiation in nonlinear composite materials, often referred to as metamaterials, is a fundamental challenge in nonlinear solid mechanics. Microstructural failure mechanisms encompass fracture, decohesion, cavitation, compression-induced contact, and instabilities, affecting their unconventional static and dynamic performances. To fully take advantage of these materials, especially in extreme applications, it is imperative to predict their nonlinear behavior using reliable, accurate, and computationally efficient numerical methodologies. This study presents an innovative nonlinear homogenization-based theoretical framework for characterizing the failure behavior of periodic reinforced hyperelastic composites induced by reinforcement/matrix decohesion and interaction between contact mechanisms and microscopic instabilities. Debonding and unilateral contact between different phases are incorporated by employing an enhanced cohesive/contact model, which features a special nonlinear interface constitutive law and an accurate contact formulation within the context of finite strain continuum mechanics. The theoretical formulation is demonstrated using periodically layered composites subjected to macroscopic compressive loading conditions along the lamination direction. Numerical results illustrate the way in which debonding phenomena, in conjunction with fiber microbuckling, may influence the critical loads of the examined composite solid. The sensitivity of the results obtained through the proposed contact-cohesive model at finite strain with respect to its implementation is also explored.

1.Introduction

The onset of failure prediction in finitely strained nonlinear composite materials, such as fiber or particle-reinforced elastomers with periodic microstructures frequently embedding voids or imperfections, is a challenging problem of fundamental interest in nonlinear solid mechanics. Since their microstructures can be tailored to obtain unusual as well as enhanced static and dynamic properties, and often incorporating multifunctional properties arising from coupling between mechanical and electrical, thermal and/or chemical characteristics (see [1,2], for instance), they are frequently referred to as metamaterials and adopted in a

*Fabrizio Greco (fabrizio.greco@unical.it).

†Present Department Civil Engineering, University of Calabria, Rende (CS), Italy

considerable number of advanced technological applications in large deformations contexts. In the last decade, the role of additive manufacturing in metamaterial research has gained significant importance enabling the production of digitally designed complex microstructures by using metal, polymeric, ceramic, biocompatible, and bioinspired materials with highly versatile performances [3–5].

The adoption of biocompatible and bioinspired metamaterials is often associated with medical applications, but not limited to, where highly deformable biocompatible materials are typically used for prosthetics, implantable medical devices, artificial tissues, and more. Biocompatibility is important in these applications but the ability of these materials to be highly deformable is essential since the materials need to conform to the shapes and movements of the human body. For instance, in implantable medical devices or prosthetics, the adopted metamaterials must be capable of withstanding large deformations and mechanical stresses without undergoing damage. In this context, the combination of advanced numerical models, able to investigate the nonlinear behavior of highly deformable metamaterials, together with the capabilities of additive manufacturing to produce custom-designed metamaterial samples that can incorporate controlled defects and features, is the best way to bridge the gap between theory and practical experimentation. This convergence among theoretical approaches, innovative methodologies, and advanced manufacturing techniques is essential for realizing the full potential of metamaterials and harnessing their unique properties for a multitude of engineering applications.

In light of these considerations, the theoretical knowledge of the involved phenomena and the capability of modeling the potential damage mechanisms, that these materials can manifest when subjected to large deformations, becomes a crucial engineering aspect in numerous fields of application. Such nonlinear phenomena, frequently occurring at the microstructural level and drastically influencing the metamaterial macroscopic behavior consist of fracture phenomena, decohesion at the interfaces between different microconstituents, matrix cavitation, contact under compression, and instabilities that can compromise the unconventional characteristics and multifunctionality of the metamaterials. Moreover, there has been a growing interest in investigating the dynamic and wave propagation characteristics of periodic microstructured metamaterials [6,7]. This interest arises from the periodicity of the microstructure, which can intrinsically influence the propagation of elastic waves. However, it is worth noting that the combination of high deformations and the onset of microscopic instabilities makes it necessary to carefully address the complexities associated with contact mechanics and damage/fracture mechanics under conditions of finite deformations, from both static and dynamic points of view.

In the past few years, to effectively address these issues from the numerical point of view and avoid computationally demanding numerical simulations, researchers proposed reliable and accurate modeling strategies based on nonlinear homogenization [8,9] and multiscale [10] techniques in a finite deformation framework. Specifically, the application of multiscale techniques in the context of microstructural arrangements was taken into account to address the limitations of the first-order homogenization approaches. For instance, in [11,12] the instability phenomena at various length scales in hyperelastic composite materials together with the effects of constitutive and geometrical nonlinearities were investigated. In [13] was highlighted that the prediction of the onset of local instability in composite materials often demands large computational effort. This arises from the direct finite element discretization of a unit cell assembly of unknown size or the use of advanced techniques like Bloch wave stability analysis [14,15], except when the instability mode has a significantly longer wavelength compared to the characteristic size of the microstructure, for which a simplified analysis based on loss of ellipticity condition can be applied. In [16] a multiscale finite element scheme was applied to analyze the coupled effects of microcracks and instability in the context of heterogeneous solid materials. Furthermore, failure arising from fiber microbuckling is a common issue in unidirectional fiber-reinforced composite materials under compression along the fiber direction (see [17,18], for additional details). This type of failure may induce microcrack initiation and propagation that significantly reduces their compressive strength due to increased energy release at crack tips especially in combination with instability phenomena. A similar phenomenon, known as buckling-induced debonding or delamination buckling, can occur in structural components reinforced with composite materials or composite laminates [19,20]. Therefore, it is important to conduct a thorough examination of the interplay between microcracks and local fiber buckling to mitigate their adverse effects on the failure behavior of fiber-reinforced composites. To the best of the authors' knowledge, the study of the nonlinear behavior of 3D printed microstructured metamaterials, considering damage and instability phenomena, represents a relatively new and emerging research field. This underscores the potential for further research and innovation in this area, as it holds significant promise for applications across various scientific disciplines. To this end, this paper proposes an original theoretical approach for modeling the failure behavior of hyperelastic layered composites as a consequence of fiber/matrix decohesion and contact mechanisms in coupling with microscopic instability phenomena.

2. Theoretical setting of the microstructural failure problem

The examined representative volume element (RVE) of a periodic composite microstructure occupies the domain $V_{(i)}$ (with boundary $\partial V_{(i)}$) in its initial undeformed configuration and contains internal cohesive/contact interfaces $\Gamma_{ch(i)}$ comprising pairs of coincident physical surfaces. The deformation process is described by the time-like parameter t, family of deformations $\boldsymbol{x}(\boldsymbol{X},t)=\boldsymbol{X}+\boldsymbol{u}(\boldsymbol{X}):V_{(i)}\rightarrow V_t$ mapping points $\boldsymbol{X}$ of the initial configuration $V_{(i)}$ into points $\boldsymbol{x}$ of the current configuration V_t, with $t=0$ corresponding to $V_{(i)}$ and $\boldsymbol{u}(\boldsymbol{X})$ being the displacement field vector.

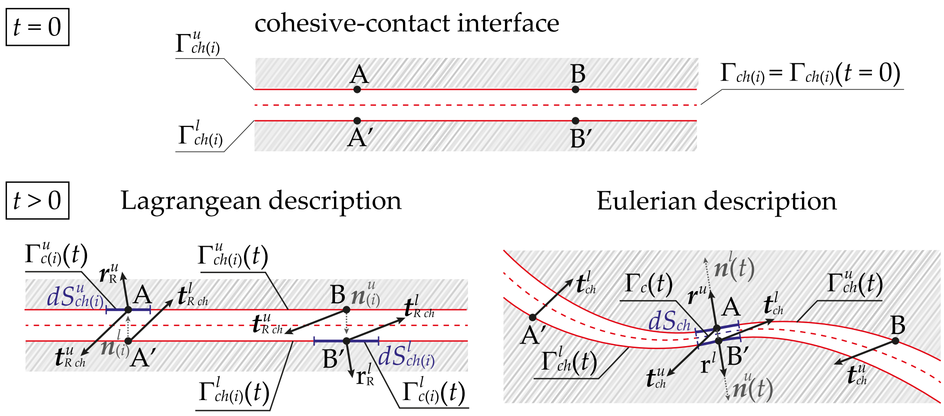

Figure 1: Kinematical description of the cohesive-contact interfaces and related surface pairs during the deformation process: a) initial undeformed configuration; b) Lagrangean description; c) Eulerian description. (A,A′) and (B,B′) are cohesive points pair while (A,B′) is a contact points pair.

As reported in Figure 1, according to a Lagrangean description, the set of cohesive interfaces in V_t are denoted by $\Gamma_{ch(i)}(t)$ (in the reference configuration $\Gamma_{ch(i)}=\Gamma_{ch(i)}(t=0)$) and comprise pairs of coincident lower and upper reference cohesive surfaces $\Gamma^l_{ch(i)}(t)$ and $\Gamma^u_{ch(i)}(t)$, respectively placed on the positive and negative side of $\Gamma_{ch(i)}(t)$ oriented by its unit normal $\boldsymbol{n}^l_{(i)}$, separating after deformation into the disjoint current cohesive surfaces $\Gamma^l_{ch}(t)$ and $\Gamma^u_{ch}(t)$. On the other hand the portions $\Gamma^l_{ch(i)}(t)$ and $\Gamma^u_{ch(i)}(t)$ where contact occurs at time t are generally disjoint and respectively denoted by the reference surface pair $\Gamma^l_{c(i)}(t)$ and $\Gamma^u_{c(i)}(t)$, since pair of points in contact in the current configuration are generally not coincident in the reference one; in the current configuration the intersection of physical surfaces pairs where contact occurs, coinciding with a single interface, is denoted by the symbol $\Gamma_c(t)$. In the following, the dependence on t will be omitted from explicit consideration in order to simplify the notation unless where it is needed to avoid ambiguity.

2.1 Contact-cohesive interface modeling

The displacement jump vector across the cohesive-contact interface at a generic cohesive point pair $(\boldsymbol{X}^l,\boldsymbol{X}^u)_{ch(i)} = \{\boldsymbol{X}^l \in \Gamma^l_{ch(i)}, \boldsymbol{X}^u \in \Gamma^u_{ch(i)} \mid \boldsymbol{X}^l = \boldsymbol{X}^u\}$ is defined as:

$$\boldsymbol{\Delta}[(\boldsymbol{X}^l,\boldsymbol{X}^u)_{ch(i)},t] = -[\![\boldsymbol{u}(\boldsymbol{X},t)]\!]_{\Gamma ch(i)} = \boldsymbol{u}(\boldsymbol{X}^u,t) - \boldsymbol{u}(\boldsymbol{X}^l,t). \tag{1}$$

With reference to the current unit normal $\boldsymbol{n}^l(t)$ to $\Gamma^l_{ch}(t)$, obtained as the transformation by the deformation mapping of $\boldsymbol{n}^l_{(i)}$, $\boldsymbol{\Delta}$ can be decomposed, respectively, into normal and tangential component vectors $\Delta_n\boldsymbol{n}^l$ and $\boldsymbol{\Delta}_s$ according to:

$$\boldsymbol{\Delta} = \Delta_n\boldsymbol{n}^l + \boldsymbol{\Delta}_s,\ \ \Delta_n = \boldsymbol{\Delta}\bullet\boldsymbol{n}^l,\ \ \boldsymbol{\Delta}_s = \left(\boldsymbol{I} - \boldsymbol{n}^l \otimes \boldsymbol{n}^l\right)\boldsymbol{\Delta}. \tag{2}$$

The following continuity-like condition for the nominal cohesive traction vector across the undeformed cohesive interface $\Gamma_{ch(i)}$ is usually assumed (see, for instance, [21–23] and the references cited therein), leading to

$$\boldsymbol{t}^l_{R\ ch} = -\boldsymbol{t}^u_{R\ ch} \quad \forall\left(\boldsymbol{X}^l,\boldsymbol{X}^u\right)_{ch(i)}, \tag{3}$$

where $\boldsymbol{t}^l_{R\ ch}(\boldsymbol{t}^u_{R\ ch})$ is the cohesive traction acting at the lower (upper) cohesive surface. The above physically-based choice of the local basis for the decomposition $\boldsymbol{\Delta}$, accounting for interface rotations, is consistent with objectivity and contact mechanics requirements, although different choices can be assumed such as the conventional one based on the deformed cohesive "mid-surface" (see [22,23], for instance). Although displacements may remain arbitrarily large, the hypothesis of small cohesive interface displacement jumps, commonly satisfied until complete decohesion takes place, implies a negligible influence of the orientation of the local basis on the cohesive behavior.

In the present study the phenomenological interface traction-separation law introduced in [21], incorporating an approximated penalty-like local contact condition, is enhanced by adopting a full finite interface deformation formulation for modeling both cohesive and contact interface phenomena, thus generalizing previous some authors' works (e.g. [24,25]). After introducing the normal and tangential cohesive interface traction component vectors, respectively denoted by $t_{n\ ch}\boldsymbol{n}^l$ and $\boldsymbol{t}_{s\ ch}$, as follows:

$$\boldsymbol{t}_{R\ ch} = \mathrm{t}_{n\ ch}\boldsymbol{n}^l + \boldsymbol{t}_{s\ ch},\ \ t_{n\ ch} = \boldsymbol{t}_{R\ ch}\bullet\boldsymbol{n}^l,\ \ \boldsymbol{t}_{s\ ch} = \left(\boldsymbol{I} - \boldsymbol{n}^l \otimes \boldsymbol{n}^l\right)\boldsymbol{t}_{R\ ch}, \tag{4}$$

where $\boldsymbol{t}_{R\ ch}$ here and in what follows denotes $\boldsymbol{t}^l_{R\ ch}$, the cohesive interface constitutive law can be written in the following form:

$$\begin{gathered}\hat{\Delta} = \sqrt{\left(\frac{\Delta_n}{\Delta_n^c}\right)^2 + \left(\frac{\|\boldsymbol{\Delta}_s\|}{\Delta_s^c}\right)^2},\quad f\left(\hat{\Delta}\right) = \frac{27}{4}t_{\max}\left(1 - 2\hat{\Delta} + \hat{\Delta}^2\right)\ \ 0 \le \hat{\Delta} \le 1,\ \hat{\Delta}_{\max}(t) = \sup_{\tau\le t}\hat{\Delta}(\tau),\\ t_{n\ ch} = \frac{\Delta_n}{\Delta_n^c}f\left(\hat{\Delta}_{\max}\right),\ \boldsymbol{t}_{s\ ch} = \alpha\frac{1}{\Delta_s^c}f\left(\hat{\Delta}_{\max}\right)\boldsymbol{\Delta}_s\end{gathered} \tag{5}$$

where Δ_n^c and Δ_s^c are the normal and tangential critical displacements, $t_{\max}$ is the normal maximum traction, $\hat{\Delta}$ is the dimensionless effective separation, $\hat{\Delta}_{\max}$ is the maximum attained by $\hat{\Delta}$ during a given deformation history, $f(\hat{\Delta})$ specifies the nonlinear variation of the normal traction in purely normal separation, and α gives the normal to tangential maximum traction ratio.

When contact is detected between cohesive surfaces, a purely tangential separation specialization of the cohesive interface law (5) is obtained by taking $\Delta_n = 0$:

$$\text{if contact occurs } (\Delta_n = 0)\quad \hat{\Delta} = \left|\frac{\|\boldsymbol{\Delta}_s\|}{\Delta_s^c}\right|,\ \ t_n^{ch} = 0,\ \ \boldsymbol{t}_s^{ch} = \alpha\frac{\boldsymbol{\Delta}_s}{\Delta_s^c}f\left(\hat{\Delta}_{\max}\right). \tag{6}$$

As a matter of fact, adopting a global full finite deformation approach to model contact at a cohesive interface outside the local cohesive law, in the presence of small cohesive interface tangential displacement jumps contact can be detected when $\Delta_n = 0$ since the interface normal relative displacement remains unchanged when determined both at a cohesive and contact points pair, namely $[\![u_n]\!]_{\Gamma ch(i)} = [\![u_n]\!]_{\Gamma c}$, where the double bracket with the subscript Γ_c denotes the jump for a contact interface material point pair $\left(\boldsymbol{X}^l, \boldsymbol{X}^u\right)_c = \left\{\boldsymbol{X}^l \in \Gamma^l_{ch(i)}, \boldsymbol{X}^u \in \Gamma^u_{ch(i)} \mid \boldsymbol{x}(\boldsymbol{X}^l, \mathrm{t}) = \boldsymbol{x}(\boldsymbol{X}^u, t)\right\}$, computed as $[\![f(\boldsymbol{X})]\!]_{\Gamma c} = f\left(\boldsymbol{X}^l\right) - f\left(\boldsymbol{X}^u\right)$. Note that when interface tangential displacement jumps are not small, the approximate cohesive interfacial interpenetration condition based on Δ_n does not imply approximations in the large deformation contact mechanics approach since contact is modeled independently from the cohesive interface model.

The rate version of the cohesive law (5) can be cast in the following form:

$$\dot{\boldsymbol{t}}_{R\,ch} = \dot{t}_{n\,ch}\boldsymbol{n}^l + t_{n\,ch}\dot{\boldsymbol{n}}^l + \dot{\boldsymbol{t}}_{s\,ch},$$
$$\dot{t}_{n\,ch} = \frac{\dot{\Delta}_n}{\Delta_n^c} f\left(\hat{\Delta}_{\max}\right) + \frac{\Delta_n}{\Delta_n^c} f'\left(\hat{\Delta}_{\max}\right)\dot{\hat{\Delta}}_{\max}, \quad \dot{\boldsymbol{t}}_{s\,ch} = \alpha\frac{\dot{\boldsymbol{\Delta}}_s}{\Delta_s^c} f\left(\hat{\Delta}_{\max}\right) + \alpha\frac{\boldsymbol{\Delta}_s}{\Delta_s^c} f'\left(\hat{\Delta}_{\max}\right)\dot{\hat{\Delta}}_{\max}, \tag{7}$$

where a dot denotes the derivative with respect to t and the prime denotes the differentiation, $\dot{\boldsymbol{n}}^l = -\left(\boldsymbol{L}^T - L_n\boldsymbol{1}\right)\boldsymbol{n}^l$, $\boldsymbol{L} = \nabla_x\dot{\boldsymbol{u}}$ is the spatial gradient (namely with respect to $\boldsymbol{x}$) of the displacement rate, also called the Eulerian velocity gradient and $L_n = \boldsymbol{Ln}\bullet\boldsymbol{n}$. It is worth noting that under contact conditions (7) leads to a zero $\dot{t}_{n\,ch}$ for both effective $(\sigma_R < 0)$ and grazing contact $(\sigma_R = 0)$ conditions, as in both the above circumstances we have that $\Delta_n = \dot{\Delta}_n = 0$.

2.2 Rate equilibrium problem and homogenized rate response

For the sake of brevity, only the equilibrium conditions at the cohesive-contact interface are here presented. The remaining equations of the equilibrium boundary value problem of the microstructure under periodic fluctuation conditions and accounting for unilateral self-contact constraints at discontinuity interfaces, can be obtained by an appropriate generalization of the formulation developed in previous authors' works [24,25]. Therefore, at a contact pair $(\boldsymbol{X}^l, \boldsymbol{X}^u)_c$ the Lagrangean form of the balance of linear momentum across the deformed cohesive-contact interface can be expressed as

$$[\![\boldsymbol{T}_R\left(dS_{ch(i)}/dS_{ch}\right)]\!]_{\Gamma c}\,\boldsymbol{n}^l_{(i)} = \boldsymbol{t}^u_{R\,ch}\left(dS^u_{ch(i)}/dS_{ch}\right) + \boldsymbol{t}^l_{R\,ch}\left(dS^l_{ch(i)}/dS_{ch}\right), \tag{8}$$

where $\boldsymbol{n}^l_{(i)}$ is the reference outward normal to the lower cohesive surface, $\boldsymbol{T}_R$ is the first Piola-Kirchhoff stress tensor, $dS^u_{ch(i)}$ and $dS^l_{ch(i)}$ respectively are the reference cohesive upper and lower surface elements (centered at $\boldsymbol{X}^l$ and $\boldsymbol{X}^u$) which are deformed in the same current surface element $dS_{ch} = dS^u_{ch} = dS^l_{ch}$ and they are related by the following relation $dS^{u/l}_{ch(i)} = J^{-1}\left\|\boldsymbol{F}^{-T}\boldsymbol{n}^{u/l}_{(i)}\right\|^{-1} dS_{ch}$. On the other hand, the local equilibrium conditions at the lower and upper contact-cohesive surfaces in the current configuration, lead to:

$$\boldsymbol{r}^l_R(\boldsymbol{X}^l) = \boldsymbol{T}_R(\boldsymbol{X}^l)\boldsymbol{n}^l_{(i)} - \boldsymbol{t}^l_{R\,ch}(\boldsymbol{X}^l)\ \forall\boldsymbol{X}^l \in \Gamma^l_{ch(i)} \text{ and } \boldsymbol{r}^u_R(\boldsymbol{X}^u) = \boldsymbol{T}_R(\boldsymbol{X}^u)\boldsymbol{n}^u_{(i)} - \boldsymbol{t}^u_{R\,ch}(\boldsymbol{X}^u)\forall\boldsymbol{X}^u \in \Gamma^u_{ch(i)}, \tag{9}$$

where $\boldsymbol{r}^l_R$ and $\boldsymbol{r}^u_R$ are the lower and upper surface nominal contact reactions, respectively, which, owing to the frictionless assumptions, can be written as $\boldsymbol{r}^l_R = \sigma^l_R\boldsymbol{n}^l$ and $\boldsymbol{r}^u_R = \sigma^u_R\boldsymbol{n}^u$, while $\sigma^l_R = (\sigma^u_R)$ being the normal nominal contact reaction on the lower (upper) crack surface. Moreover $\boldsymbol{T}_R(\boldsymbol{X}^i)\boldsymbol{n}^i_{(i)} = \boldsymbol{t}^i_R$ with $i = u, l$ is the nominal traction vector at the upper and lower cohesive surfaces. An appropriate combination of eqs (9) written for a contact points pair $(\boldsymbol{X}^l, \boldsymbol{X}^u)_c$, after the use of eqn (8), leads to the following relation:

$$\sigma^u_R dS^u_{ch(i)}/dS_{ch} = \sigma^l_R dS^l_{ch(i)}/dS_{ch} = \sigma \quad \forall(\boldsymbol{X}^l, \boldsymbol{X}^u)_c \tag{10}$$

where σ is the corresponding true normal contact reaction and dS_{ch} is the current surface element centered at the current position of the contact points pair obtained as the transformation of its reference counterpart through the Nanson's formula. It follows that the nominal contact pressure on the upper and lower cohesive-contact surfaces can be determined as $\sigma^i_R = \boldsymbol{T}_R(\boldsymbol{X}^i)\boldsymbol{n}^i_{(i)}\cdot\boldsymbol{n}^i - \boldsymbol{t}^i_{R\,ch}\cdot\boldsymbol{n}^i$ with $i = u, l$.

Each solid phase of the RVE obeys an incrementally linear constitutive law $\dot{\boldsymbol{T}}_R = \boldsymbol{C}^R(\boldsymbol{X}, \boldsymbol{F})[\dot{\boldsymbol{F}}]$, where $\boldsymbol{C}^R(\boldsymbol{X}, \boldsymbol{F})$ is assumed symmetric to encompasses hyperelastic materials for which $C^R_{ijkl} = \partial^2 W(\boldsymbol{X}, \boldsymbol{F})/\partial F_{ij}\partial F_{kl}$ with $W(\boldsymbol{X}, \boldsymbol{F})$ the strain energy-density function of each phase. In order to carry out uniqueness and stability analyses along the principal equilibrium path driven by a macroscopic deformation process $\bar{\boldsymbol{F}}(t)$, where $\bar{\boldsymbol{F}}(t)=1/|V_{(i)}|\int_{\partial V_{(i)}}\boldsymbol{x}(\boldsymbol{X},t)\otimes\boldsymbol{n}_{(i)}dS_{(i)}$, the equations governing the RVE quasi-static rate response to a macroscopic deformation gradient rate $\dot{\bar{\boldsymbol{F}}}$ superposed at the generic time t must be considered. To this aim an appropriate extension of the asymptotic analysis developed in [25] can be performed. In particular, the rate interface contact conditions can be written as:

$$[\![\dot{u}_n(\boldsymbol{X})]\!]_{\Gamma_C}\leq 0,\ \sigma_R^u[\![\dot{u}_n(\boldsymbol{X})]\!]_{\Gamma_C}=0,\ \dot{\sigma}_R^u\leq 0 \text{ and } \dot{\sigma}_R^u[\![\dot{u}_n(\boldsymbol{X})]\!]_{\Gamma_C}=0 \text{ if } \sigma_R^u=0, \forall\left(\boldsymbol{X}^u,\boldsymbol{X}^l\right)_C \tag{11}$$

where the subscript n denotes projection on $\boldsymbol{n}^l$ and, considering the additive decomposition $\boldsymbol{x}(\boldsymbol{X},t)=\bar{\boldsymbol{F}}(t)\boldsymbol{X}+\boldsymbol{w}(\boldsymbol{X},t)$, the normal displacement rate jump can be expressed as a function of the periodic fluctuation field rate $\dot{\boldsymbol{w}}(\boldsymbol{X})$ in the following form $[\![\dot{u}_n(\boldsymbol{X})]\!]_{\Gamma_c}=[\![\dot{w}_n(\boldsymbol{X})]\!]_{\Gamma_C}-\boldsymbol{n}^l\bullet[\dot{\bar{\boldsymbol{F}}}(\boldsymbol{X}^u-\boldsymbol{X}^l)]$. In addition, eqs (8) and (9) give the following rate equilibrium conditions at the actual cohesive contact interface Γ^c:

$$\begin{cases}\dot{\boldsymbol{r}}_R{}^u\left(dS^u_{ch(i)}/dS_{ch}\right)+\dot{\boldsymbol{r}}_R{}^l\left(dS^l_{ch(i)}/dS_{ch}\right)+\ \sigma_R{}^u\boldsymbol{n}^u\left(dS^u_{ch(i)}/dS_{ch}\right)^{\bullet}+\sigma_R{}^l\boldsymbol{n}^l\left(dS^l_{ch(i)}/dS_{ch}\right)^{\bullet}=\boldsymbol{0}\\ \dot{\boldsymbol{t}}_R^A-\dot{\boldsymbol{t}}_{R\,ch}^A=\sigma_R^A\dot{\boldsymbol{n}}^A+\dot{\sigma}_R^A\boldsymbol{n}^A\\ \dot{\boldsymbol{t}}_R^{B'}-\dot{\boldsymbol{t}}_{R\,ch}^{B'}=\sigma_R^{B'}\dot{\boldsymbol{n}}^{B'}+\dot{\sigma}_R^{B'}\boldsymbol{n}^{B'}\end{cases}\qquad \forall(\boldsymbol{X}^l,\boldsymbol{X}^u)_c\ , \tag{12}$$

The solution of the RVE rate equilibrium problem leads to obtain a homogeneous of degree one implicit nonlinear tensorial relationship between $\dot{\bar{\boldsymbol{F}}}$ and the macroscopic nominal stress tensor rate $\dot{\bar{\boldsymbol{T}}}_R$; consequently, the macroscopic rate constitutive relation can be written as

$$\dot{\bar{\boldsymbol{T}}}_R=\bar{\boldsymbol{C}}^R(\dot{\bar{\boldsymbol{F}}})[\dot{\bar{\boldsymbol{F}}}], \tag{13}$$

where $\bar{\boldsymbol{T}}_R(t)=1/|V_{(i)}|\int_{\partial V_{(i)}}\boldsymbol{t}_R(\boldsymbol{X},t)\otimes\boldsymbol{X}dS_{(i)}$. When effective contact occurs and the rate cohesive law is linear, the rate homogenized constitutive law turns out to be a linear one and can be defined in terms of the homogenized nominal moduli tensor $\bar{\boldsymbol{C}}^R$ as $\dot{\bar{\boldsymbol{T}}}_R=\bar{\boldsymbol{C}}^R[\dot{\bar{\boldsymbol{F}}}]$.

A classical macroscopic condition for the stability of the periodic solid corresponds to the following strong ellipticity of the one-cell homogenized moduli tensor, coinciding with the positive definiteness of the one-cell acoustic tensor $\bar{\boldsymbol{Q}}$:

$$\Lambda\left(\bar{\boldsymbol{F}}(t),\dot{\bar{\boldsymbol{F}}}\right)=\min_{\|\bar{\boldsymbol{m}}\|=\|\bar{\boldsymbol{N}}\|=1}\left\{\bar{\boldsymbol{C}}^R\left(\dot{\bar{\boldsymbol{F}}}\right)(\bar{\boldsymbol{m}}\otimes\bar{\boldsymbol{N}})\bullet\bar{\boldsymbol{m}}\otimes\bar{\boldsymbol{N}}\right\}=\min_{\|\bar{\boldsymbol{m}}\|=\|\bar{\boldsymbol{N}}\|=1}\left\{\bar{\boldsymbol{Q}}\left(\dot{\bar{\boldsymbol{F}}},\bar{\boldsymbol{N}}\right)(\bar{\boldsymbol{m}})\bullet\bar{\boldsymbol{m}}\right\}>0\ . \tag{14}$$

2.3 Stability and uniqueness issues: exact and approximate interface formulations

The stability functional can be cast in the following form:

$$S\left(\bar{\boldsymbol{F}},\dot{\boldsymbol{w}}\right)=\int_{B_{(i)}}\boldsymbol{C}^R\left(\boldsymbol{X},\bar{\boldsymbol{F}}\right)[\nabla\dot{\boldsymbol{w}}]\bullet\nabla\dot{\boldsymbol{w}}dV_{(i)}-\int_{\Gamma_{c(i)}{}^l}\sigma_R^l\dot{\boldsymbol{n}}^l\cdot[\![\dot{\boldsymbol{w}}]\!]_{\Gamma_c}dS^l_{(i)}+\int_{\Gamma_{c(i)}{}^l}\sigma_R{}^l\left[\!\!\left[\left(\frac{dS_{(i)}}{dS}\right)^{\bullet}\frac{dS}{dS_{(i)}}\right]\!\!\right]_{\Gamma_c}\dot{w}_n{}^l dS^l_{(i)}+\int_{\Gamma^l{}_{ch(i)}}\dot{\boldsymbol{t}}_{R\,ch}\cdot\dot{\boldsymbol{\Delta}}\,dS^l_{ch(i)}\ . \tag{15}$$

The positivity condition of the above-defined stability functional for all $\dot{\boldsymbol{w}}(\boldsymbol{x})\neq\boldsymbol{0}\in A^*(\bar{\boldsymbol{F}},\dot{\bar{\boldsymbol{F}}}=\boldsymbol{0})$, where $A^*(\bar{\boldsymbol{F}},\dot{\bar{\boldsymbol{F}}})$ represents the set of admissible fluctuation rates defined as

$$A^*(\bar{\boldsymbol{F}},\dot{\bar{\boldsymbol{F}}})=\left\{\dot{\boldsymbol{w}}\in H^1(V_{(i)\#})\,\middle|\,[\![\dot{u}_n]\!]_{\Gamma_C}=0 \text{ if } \sigma_R{}^u<0,\ [\![\dot{u}_n]\!]_{\Gamma_C}\leq 0 \text{ if } \sigma_R{}^u=0 \text{ on } \Gamma^l_{c(i)} \text{ and } \Gamma^u_{c(i)}\right\}, \tag{16}$$

$H^1(V_{(i)\#})$ denoting the usual Hilbert space of order one of vector-valued functions periodic over $V_{(i)}$, ensures the stability of the considered equilibrium configuration. On the other hand, a primary instability occurs at the corresponding critical loading parameter t_{cS} when the minimum eigenvalue $\Lambda = \min_{\dot{\boldsymbol{w}}(\boldsymbol{x})\in A^*(\bar{\boldsymbol{F}},\dot{\bar{\boldsymbol{F}}}=\boldsymbol{0})} \left\{ S(\bar{\boldsymbol{F}},\dot{\boldsymbol{w}}) / \int_{B_{(i)}} \nabla\dot{\boldsymbol{w}}\bullet\nabla\dot{\boldsymbol{w}}\, dV_{(i)} \right\}$ first vanishes.

Assuming a homogeneous macroscopic incremental loading ($\dot{\bar{\boldsymbol{F}}} = \boldsymbol{0}$), the stability condition based on eqn (15) implies incremental uniqueness, however, owing to the absence of a variational structure, the primary eigenstate loading level t_{cE}, corresponding to a primary bifurcation for homogenous data $\dot{\bar{\boldsymbol{F}}} = \boldsymbol{0}$, does not precede the primary instability one, i.e. $t_{cS} \le t_{cE}$. Moreover, when contact rate loading terms and the rate cohesive model admit a potential, a special situation examined in the subsequent part of the paper, primary instability and eigenstate critical load levels coincide, i.e. $t_{cS} = t_{cE}$.

For the general rate problem driven by a non-homogeneous macroscopic incremental loading $\dot{\bar{\boldsymbol{F}}}_{(0)} \neq \boldsymbol{0}$, the above connections between primary instability and primary bifurcation (with the corresponding loading level referred to as t_c) are not valid as a consequence of the conditionality nature of self-contact unilateral contact terms and of the nonlinearities in the cohesive incremental constitutive law. However, when the displacement discontinuity interface is everywhere under effective contact condition ($\sigma < 0\ \forall \boldsymbol{x} \in \Gamma_C$), reducing unilateral contact conditions to linear constraints ($[\![\dot{u}_n]\!]_{\Gamma_C} = 0$ on Γ_C), and the cohesive rate model is linear, the connections obtained for homogeneous macroscopic incremental loading still apply for the non-homogeneous macroscopic loading case $\dot{\bar{\boldsymbol{F}}}_{(0)} \neq \boldsymbol{0}$, namely $t_{cS} \le t_{cE}$ and $t_c = t_{cE}$, where t_c is the primary bifurcation loading level. If the contact rate loading terms and the rate cohesive model admit a potential, a special situation examined in the numerical applications of the paper, primary instability and bifurcation critical load levels coincide, i.e. $t_{cS} = t_c$.

A first simplified cohesive-contact model can be introduced in which the third contribution in eqn (15) is neglected according to the hypotheses of small cohesive surface relative deformations (but large interface displacements are allowed). This leads to the following modified stability functional:

$$
\begin{gathered}
S'(\bar{\boldsymbol{F}},\dot{\boldsymbol{w}}) = \int_{V_{(i)}} \boldsymbol{C}^R(\boldsymbol{X},\bar{\boldsymbol{F}})[\nabla\dot{\boldsymbol{w}}]\cdot\nabla\dot{\boldsymbol{w}}\, dV_{(i)} - \int_{\Gamma^l_{c(i)}} \sigma^l_R \dot{\boldsymbol{n}}^l \cdot [\![\dot{\boldsymbol{w}}]\!]_{\Gamma_{c(i)}}\, dS^l_{(i)} + \int_{\Gamma^l_{ch(i)}} \dot{\boldsymbol{t}}_{R\,ch} \cdot \dot{\boldsymbol{\Delta}}\, dS^l_{ch(i)} \quad \forall \dot{\boldsymbol{w}}(\boldsymbol{x}) \neq \boldsymbol{0} \in A'\ (\bar{\boldsymbol{F}}, \dot{\bar{\boldsymbol{F}}} = \boldsymbol{0}) \\
A'(\bar{\boldsymbol{F}},\dot{\bar{\boldsymbol{F}}}) = \left\{ \dot{\boldsymbol{w}} \in H^1(V_{(i)\#}) \,\middle|\, [\![\dot{u}_n]\!]_{\Gamma_{ch(i)}} = 0 \text{ if } \sigma_R{}^u < 0,\ [\![\dot{u}_n]\!]_{\Gamma_{ch(i)}} \le 0 \text{ if } \sigma_R{}^u = 0, \text{ on } \Gamma^l_{ch(i)} \text{ and } \Gamma^u_{ch(i)} \right\}
\end{gathered}
\tag{17}
$$

The approximation is consistent with an interface equilibrium condition (8) written assuming that the current contact points pair corresponds to an initially coincident points pair, i.e. pair $(\boldsymbol{X}^l,\boldsymbol{X}^u)_{ch(i)} = (\boldsymbol{X}^l,\boldsymbol{X}^u)_c$, leading to $dS_{ch} = dS^u_{ch(i)} = dS^l_{ch(i)}$ and to the continuity condition for the nominal traction vector across the undeformed contact-cohesive interface.

When surface rotations at the contact-cohesive interfaces are also neglected according to small displacements hypotheses at the cohesive interface, a second simplified cohesive-contact model is obtained and the above functional further simplifies in:

$$
S''(\bar{\boldsymbol{F}},\dot{\boldsymbol{w}}) = \int_{B_{(i)}} \boldsymbol{C}^R(\boldsymbol{X},\bar{\boldsymbol{F}})[\nabla\dot{\boldsymbol{w}}]\cdot\nabla\dot{\boldsymbol{w}}\, dV_{(i)} + \int_{\Gamma^l_{ch(i)}} \dot{\boldsymbol{t}}_{R\,ch} \cdot \dot{\boldsymbol{\Delta}}\, dS^l_{ch(i)} \quad \forall \dot{\boldsymbol{w}}(\boldsymbol{x}) \neq \boldsymbol{0} \in A'\ (\bar{\boldsymbol{F}}, \dot{\bar{\boldsymbol{F}}} = \boldsymbol{0}), \tag{18}
$$

where it must be intended that the contributions arising from the rates of the normal and tangential unit vectors in the definition of the cohesive traction rate are neglected.

In the context of the above-approximated formulations, interface contact phenomena can be locally incorporated in the cohesive law by means of a penalty formulation imposing $[\![\dot{u}_n]\!]_{\Gamma_{ch(i)}} = 0$, as done in most cases in the technical literature (see [20,21,23,26] for instance, and the reference cited therein), with the set of admissible fluctuation rates characterized by unconstrained functions along the contact interfaces, namely $A'(\bar{\boldsymbol{F}},\dot{\bar{\boldsymbol{F}}}) = \{ \dot{\boldsymbol{w}} \in H^1(V_{(i)\#}) \}$. The cohesive law (5) can be thus modified by considering that, in place of eqs (6), if $\Delta_n < 0 \rightarrow \hat{\Delta} = |\, \|\boldsymbol{\Delta}_s\| / \Delta^c_s \,|$ and $t_{n\,ch} = k_n \Delta_n$ with k_n a penalization parameter which must be chosen with a high value. Note that in some works [21,26] the above approximate treatment of unilateral cohesive interface contact has been developed with reference to the undeformed geometry of the cohesive surface ($[\![\dot{u}_{n(i)}]\!]_{\Gamma_{ch(i)}} = 0$), thus neglecting the rotations of the unit normal to the deformed cohesive surfaces as in the second approximated formulation.

3. Numerical applications

In this section, the theoretical dissertation reported above is applied to investigate, from the numerical point of view, the microbuckling phenomena inducing debonding in highly deformable 2D layered composites. The geometrical representation of the investigated RVE is shown in Figure 2, along with an example of mesh discretization based on quadratic triangular Delaunay elements. The layered RVE model consists of a reinforcing material (dark grey area) placed between two layers of matrix phases (light grey areas) and embeds cohesive interface models (red lines) at the two reinforcement/matrix interfaces. The height and length of the RVE are denoted as H and L, respectively.
The reinforcement thickness is H_r = 1 mm, and its value is related to the RVE height through the reinforcement volume fraction parameter V_f, which is equal to the ratio between H_r and H. The mechanical behavior of the layered system microconstituents is described by a hyperelastic constitutive law following the neo-Hookean energy density function:

$$W_\alpha = \frac{E_\alpha}{4(1+\upsilon_\alpha)}\left(I_1 - \ln(I_3) - 3\right) + \frac{\upsilon_\alpha E_\alpha}{2(1+\upsilon_\alpha)(1-2\upsilon_\alpha)}\left(I_3^{1/2} - 1\right)^2, \tag{19}$$

where the subscript $\alpha = m, r$ is referred to the matrix or reinforcing material, respectively, E_α denotes the Young's modulus and υ_α the Poisson ratio, both considered at the undeformed configuration. Moreover $I_1 = tr(\boldsymbol{C})$ and $I_3 = \det(\boldsymbol{C}) = J^2$ are the first and third invariant of the right Cauchy-Green tensor $\boldsymbol{C}=\boldsymbol{F}^T\boldsymbol{F}$, respectively, and $J = det\boldsymbol{F}$. The Young's modulus and the Poisson's ratio are related to the shear modulus μ_α and the first Lamè parameter λ_α at zero stress by the following relations: $\mu_\alpha = E_\alpha/[2(1+\upsilon_\alpha)]$ and $\lambda_\alpha = \upsilon_\alpha E_\alpha/[(1+\upsilon_\alpha)(1-2\upsilon_\alpha)]$. The latter, being strictly related to the so-called 3D bulk modulus $k_\alpha = \lambda_\alpha + 2\mu_\alpha/3$, governs the compressibility of the solid material. The initial Young's modulus of the matrix E_m is set equal to 1 GPa, while the one of the reinforcing material E_r is set equal to $k_E E_m$, where k_E denotes the Young's modulus stiffness ratio giving a measure of the stiffness of the reinforcing material compared with the matrix.

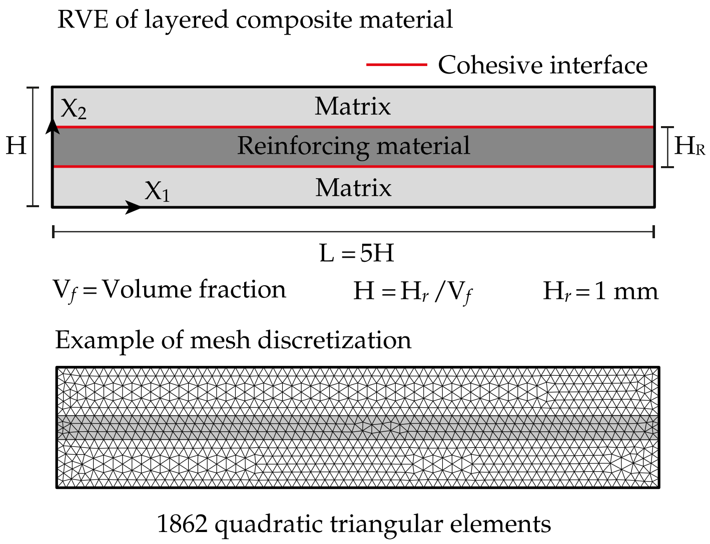

Figure 2: Geometrical representation of the investigated RVE related to a layered composite microstructure.

The numerical investigation depicted in Figures 3-5 consists of a parametric analysis performed by gradually varying the following geometrical and material parameters: the reinforcement volume fractions $V_f = 0.05;\ 0.1; 0.2$, the Young's modulus stiffness ratio $k_E = 1;\ 2; 10$, and the percentages of integrity of the cohesive interfaces $\%I = 100;\ 20; 14; 10; 4; 3$. The latter defines the percentage of equivalent displacement jump still available before the complete decohesion of the cohesive crack faces and, therefore, it is strictly related to the secant stiffness of the cohesive interfaces. The cohesive parameters required to define the traction-separation law are $t_{max} = 70$ MPa, $G_{Ic} = 9/16\ t_{max}\ \Delta_n^c = G_{IIc}$=107 J/m^2 and $\alpha = 1$, thus implying $\Delta_n^c = \Delta_s^c$ since G_{Ic}=9/16 t_{max} Δ_n^c and G_{IIc}=9/16 $\alpha\ t_{max}\ \Delta_s^c$.
The numerical procedure is based on two different steps. In the first one, periodic boundary conditions are adopted for the external boundaries of the layered composite RVE, and a uniaxial macroscopic compression load along the X_1 direction is applied to evaluate the so-called principal solution path, representing the nonlinear equilibrium solution of the RVE along the stable equilibrium path. Specifically, the following macroscopic deformation gradient tensor is applied to the RVE:

$$\overline{\boldsymbol{F}}(\lambda) = (1-t)\boldsymbol{e}_1 \otimes \boldsymbol{e}_1 + \boldsymbol{e}_2 \otimes \boldsymbol{e}_2 + \boldsymbol{e}_3 \otimes \boldsymbol{e}_3 \tag{20}$$

where t is a scalar load factor parameter whose opposite value represents, due to the absence of macroscopic rigid body rotations, the principal value of the macroscopic Biot strain tensor in the X_1 direction, while 1-t corresponds to the macroscopic principal stretch along the same direction. With reference to the uniaxial macroscopic loading path investigated in this study, the principal solution path, owing to the homogeneous properties of each constituent, exhibits constant stresses and strains within each layer, and thus the solution for the principal path in a finite deformation regime remains unaffected by the presence of the cohesive interfaces since the cohesive surfaces remain plane and undergo effective contact conditions (with a constant interface contact pressure σ) without displacement discontinuities until the initiation of the primary instability. In addition, using the periodicity condition for the fluctuation rate field and its jump $[\![\dot{\boldsymbol{w}}]\!]_{\Gamma_c}$ at the boundary points of the cohesive interface, it is possible to prove that for the examined macroscopic loading path the rate contact loading terms admit a potential. This leads to simplifying the uniqueness and stability analyses which can be both carried out by monitoring the minimum eigenvalue of the stability functional (15).
Along the examined principal solution equilibrium path, the displacement jumps across the cohesive interface vanish and initially corresponding material points pairs coincide with current contact points pairs:

$$\begin{aligned} &\boldsymbol{\Delta}[(\boldsymbol{X}^l, \boldsymbol{X}^u)_{ch(i)}, t] = \boldsymbol{0} \ \text{ with } \ 0 \le t \le t_c \\ &[\![\dot{u}_n(\boldsymbol{X})]\!]_{\Gamma C} = [\![\dot{w}_n(\boldsymbol{X})]\!]_{\Gamma_C} = [\![\dot{w}_n(\boldsymbol{X})]\!]_{\Gamma C(i)} = 0, \quad \forall (\boldsymbol{X}^u, \boldsymbol{X}^l)_c = (\boldsymbol{X}^u, \boldsymbol{X}^l)_{ch(i)} \end{aligned} \tag{21}$$

The cohesive interface rate constitutive law assumes the following simplified form:

$$\dot{\boldsymbol{t}}_R^{ch} = \dot{\boldsymbol{t}}_s^{ch}, \quad \dot{\boldsymbol{t}}_s^{ch} = \alpha \frac{\dot{\boldsymbol{\Delta}}_s}{\Delta_s^c} \frac{27}{4} t_{\max} \tag{22}$$

since $\Delta_n = 0,\ \hat{\Delta} = 0,\ \hat{\Delta}_{\max}(t) = 0,\ \boldsymbol{\Delta}_s = \boldsymbol{0}$. The cohesive contribution to the stability functional becomes:

$$\int_{\Gamma^l_{ch(i)}} \dot{\boldsymbol{t}}_{R\ ch} \bullet \dot{\boldsymbol{\Delta}}\, dS^l_{ch(i)} = \int_{\Gamma^l_{ch(i)}} \alpha \frac{\|\dot{\boldsymbol{\Delta}}_s\|^2}{\Delta_s^c} \frac{27}{4} t_{\max}\, dS^l_{ch(i)}, \tag{23}$$

where it can be noted that rate cohesive traction turns out to admit a rate potential. Consequently, when the incremental loading terms arising from self-contact are *self-adjoint*, the stability functional acting as an exclusion functional assumes a variational structure leading to the coincidence between a primary eigenstate (and thus primary bifurcation due to the linearity of both contact mechanics and cohesive model equations) and a primary instability. In addition, it can be noted that the cohesive contribution (23) *is stabilizing* since a positive definite function of $\dot{\boldsymbol{\Delta}}$. When the simplified contact model (18) is adopted, we obtain that a primary eigenstate (in turn corresponding to a primary bifurcation) coincides with a primary instability state *independently of the self-adjointness* of contact terms. As a matter of fact, the simplified stability functional assumes the following form:

$$S''(\overline{\boldsymbol{F}}, \dot{\boldsymbol{w}}) = \int_{B_{(i)}} \boldsymbol{C}^R(\boldsymbol{X}, \overline{\boldsymbol{F}})[\nabla \dot{\boldsymbol{w}}] \cdot \nabla \dot{\boldsymbol{w}}\, dV_{(i)} + 2 \int_{\Gamma^l_{ch(i)}} U(\dot{\boldsymbol{\Delta}})\, dS^l_{ch(i)} \tag{24}$$

where the rate cohesive traction potential assumes the following form $U\left(\dot{\boldsymbol{\Delta}}\right)=1/2\boldsymbol{K}_t\left[\dot{\boldsymbol{\Delta}}\right]\bullet\dot{\boldsymbol{\Delta}}=1/2k_s\dot{\Delta}_s^2$, $\dot{\Delta}_s=\left\|\dot{\boldsymbol{\Delta}}_s\right\|$ and $\boldsymbol{K}_t=k_s\left(\boldsymbol{1}-\boldsymbol{n}^l\otimes\boldsymbol{n}^l\right)$, with $k_s=\alpha\frac{1}{\Delta_s^c}\frac{27}{4}t_{\max}$.

In the second step, the stability analyses were performed by superimposing, on each step of the principal solution, a macroscopic deformation gradient rate and solving the corresponding boundary value problems in terms of the fluctuation rate field. Specifically, the microscopic primary instabilities (coinciding with a primary bifurcation), related to the Exact and the two Simplified contact-cohesive formulations, occur at the vanishing of the minimum eigenvalue associated with the stability functionals reported in Section 2.3, while the macroscopic primary instability was obtained when the at the first vanishing of the lowest eigenvalue associated with the macroscopic acoustic tensor. In the Exact formulation, a full finite deformation approach is adopted to model contact and cohesive interface constitutive laws; in the Simplified formulation I the dependence on cohesive surface deformations is neglected whereas in the Simplified formulation II the dependence on both cohesive surface deformations and rotations are omitted. In Figures 3-5, the critical load factors are reported as a function of the percentage of the integrity of the cohesive interfaces to investigate the influence of the nonlinear contributions arising on the cohesive interfaces due to the onset of primary instabilities. Specifically, the microscopic critical load factors associated with the Exact and Simplified formulations I e II are depicted with red, green, and blue solid curves, respectively, while those associated with the macroscopic instabilities are reported with black solid curves. In addition, the critical mode shapes associated with the Exact solution are illustrated for the cases in which the mode shape switches from local to global with a color map showing the norm of the displacement vector.

Figure 3 shows the critical load factors associated with a layered composite material characterized by a Young's modulus stiffness ratio $k_E=1$ that corresponds to a homogeneous solid material characterized by a couple of cohesive interfaces placed at a distance H_r = 1 mm.

We observe that, in general, the critical load factors decrease as the volume fraction increases, implying that a thicker reinforcing layer results in lower critical load factors. However, since the scenario presented in Figure 3 refers to a homogeneous solid material, we can infer that the reduction in critical load factors is primarily influenced by the thickness of the matrix layer, which defines the separation between a pair of cohesive interfaces in a perfectly periodic layered material, rather than the specific thickness of the reinforcing layer.

In Figure 3.a and 3.b, related to a volume fraction V_f equal to 0.05 and 0.1, respectively, we observe that the onset of primary instability, occurring at a percentage of integrity within the range of 100 to 10%, is characterized by a critical mode shape with wavelength comparable to the RVE length (microscopic instability).

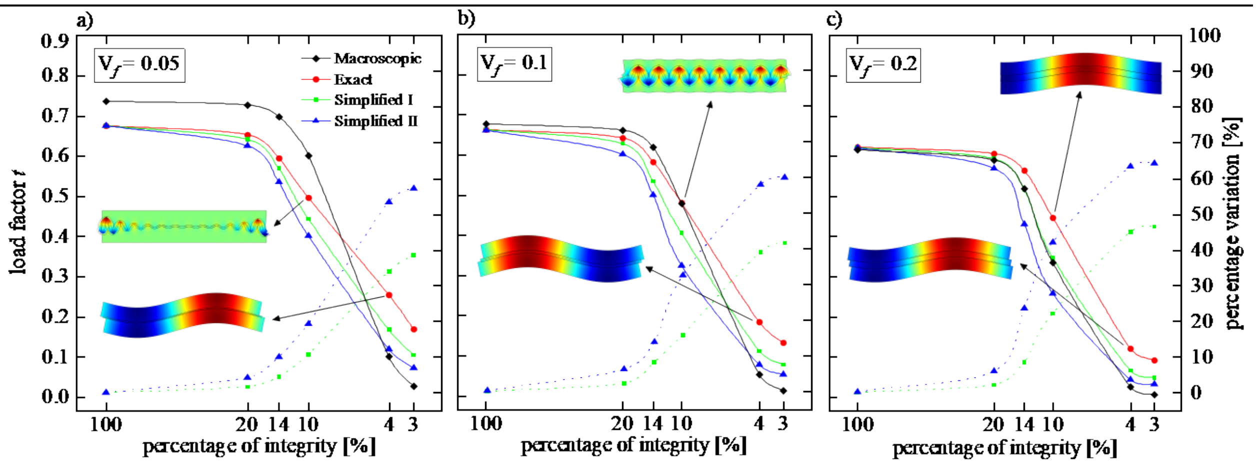

Figure 3: Microscopic critical load factors associated with the Exact (red solid curves) and the Simplified formulations (green and blue solid curves) together with the macroscopic one (black solid curves) as a function of the percentage of integrity of the cohesive interface for a layered composite material with $k_E = 1$ and $V_f = 0.05; 0.1; 0.2$ in (a), (b) and (c), respectively. The dotted curves show the percentage variation of the critical load factors associated with the Simplified formulations with respect to the Exact ones.

However, in the range from 10 to 3%, particularly at the point where the black and red curves intersect (thus leading to a macroscopic critical load level lower than the microscopic one for the examined RVE length), a transition to a critical mode shape with a longer wavelength than the RVE length is observed (a symptom of macroscopic instability). On the contrary, when $V_f = 0.2$ (as seen in Figure 3.c), we notice that the primary instability exhibits a long wavelength (indicating macroscopic instability) across all the examined percentages of integrity. In Figure 3, the percentage variations between the Exact formulation and the Simplified formulations I and II are minimal when the percentage of integrity is within the range of 100% to 20%. However, as the integrity falls below 20%, these differences become more pronounced, indicating a significant underestimation of the critical load factors across all the examined volume fractions. Specifically, this underestimation becomes particularly severe as the integrity percentage decreases, reaching its maximum peak at 64% for the Simplified Formulation II (indicated by the blue dotted curve) and 46% for the Simplified Formulation I (represented by the green dotted curve) when $V_f = 0.2$ and I% = 3. In Figure 3.c, related to a scenario of a layered material with $V_f = 0.2$, the percentage variation of critical load factors is higher compared to the cases with lower volume fractions (Figure 3.a and b) due to the onset of primary macroscopic instabilities for any examined percentage of integrity, as evident from the black curve consistently positioned below the red one.

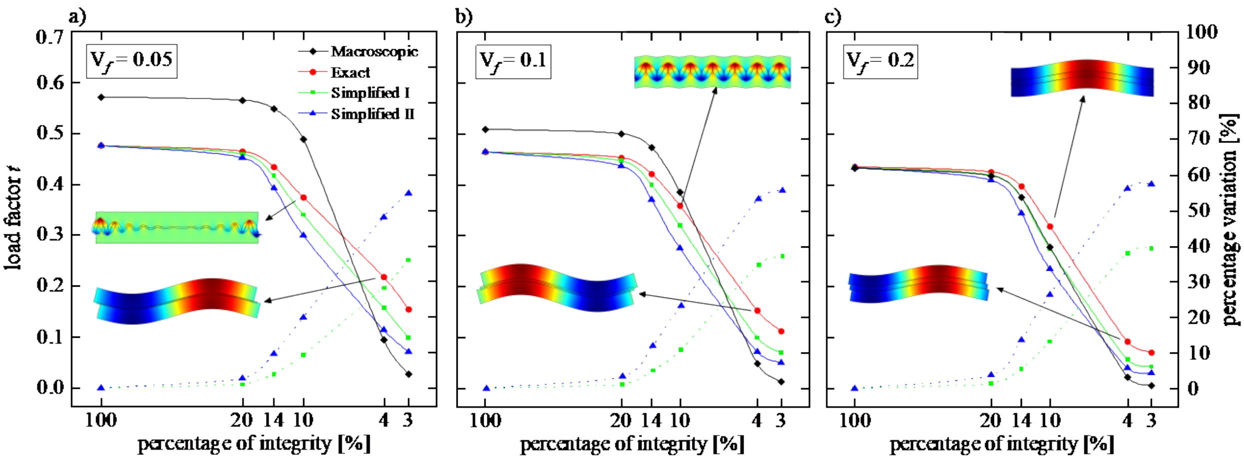

Figure 4: Microscopic critical load factors associated with the Exact (red solid curves) and the Simplified formulations (green and blue solid curves) together with the macroscopic one (black solid curves) as a function

of the percentage of integrity of the cohesive interface for a layered composite material with k_E = 2 and V_f = 0.05; 0.1; 0.2 in (a), (b) and (c), respectively. The dotted curves show the percentage variation of the critical load factors associated with the Simplified formulations with respect to the Exact ones.

In Figure 4 the critical load factors obtained for a Young's modulus stiffness ratio k_E = 2 are reported. The general trend is similar to the homogeneous material (with k_E = 1) but with a slight reduction in the critical load factors. Also in this case, for a percentage of integrity I% below 20%, severe underestimations of the critical load factors were observed with the most significant underestimations occurring in the case of I% = 3 and V_f = 0.2 (see Figure 4.c) and equal to 58% and 39% for the Simplified Formulations II and I, respectively.
Examining the critical mode shapes and the trends of the macroscopic and the exact microscopic instability curves (black and red, respectively), we observed a transition from the onset of a microscopic to a macroscopic primary instability in Figure 4.a and 4.b when the integrity ranged from 10% to 4%.

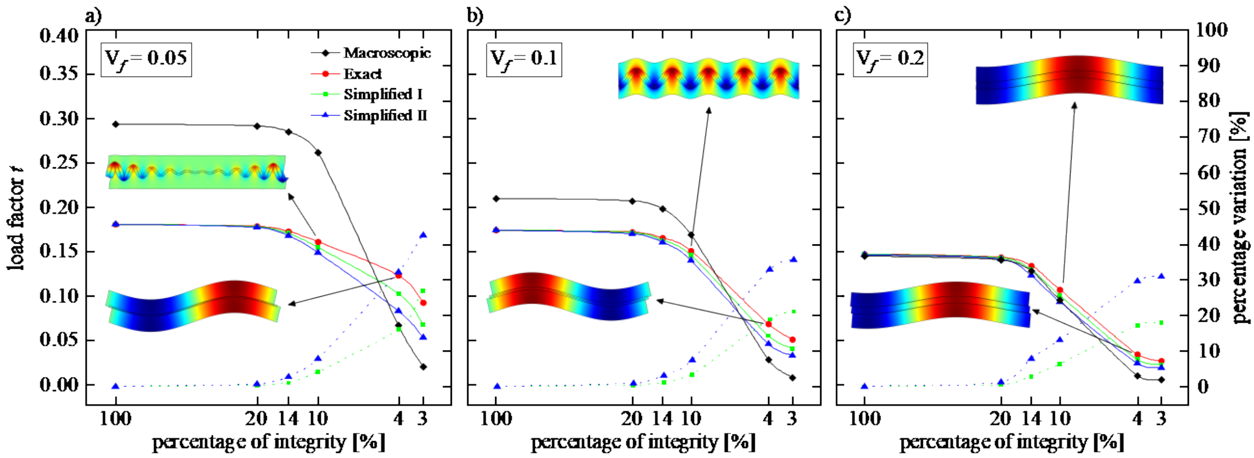

Figure 5: Microscopic critical load factors associated with the Exact (red solid curves) and the Simplified formulation (green and blue solid curves) together with the macroscopic one (black solid curves) as a function of the percentage of integrity of the cohesive interface for a layered composite material with $k_E = 10$ and $V_f = 0.05;\ 0.1;\ 0.2$ in (a), (b) and (c), respectively. The dotted curves show the percentage variation of the critical load factors associated with the Simplified formulations with respect to the Exact ones.

In Figure 5, the latest set of results related to the highest examined Young's modulus stiffness ratio, k_E = 10, are presented. Similar to the previous set of numerical findings, the critical load factors exhibit a decreasing trend as the percentage of integrity decreases. This trend remains practically constant from 100% to 20% and gradually decreases from 20% to 3%. Notably, the obtained critical load factors are lower in comparison to those associated with the earlier investigated Young's modulus stiffness ratios (i.e k_E = 1 and k_E = 2). Furthermore, there is a reduction in the percentage variation for the Simplified I and II formulations, indicating that the nonlinear contributions arising at the cohesive interfaces, due to the onset of instability, are less pronounced for layered composite materials with a high stiffness ratio between the matrix and the reinforcement. Interestingly, a reversal in the trend of underestimation of the critical load factor is observed. The maximum underestimation, which is equal to 43% for Simplified II and 28% for Simplified I, is found for the lowest examined volume fraction, V_f = 0.05 contrarily to the scenarios reported in Figures 3 and 4, in which the highest underestimations were observed for the highest examined volume fraction, V_f = 0.2.

4. Conclusions

This study introduces an innovative theoretical framework based on nonlinear homogenization to characterize the failure behavior of periodic reinforced hyperelastic composites. The focus of the work is on understanding the nonlinear effects induced by the reinforcement/matrix decohesion and its interaction with contact mechanisms and microscopic instabilities. The modeling approach incorporates debonding and unilateral contact between layers through an enhanced cohesive-contact method, employing a specific nonlinear interface constitutive law and an accurate contact formulation within the context of the finite deformation continuum mechanics.

The investigation was performed on periodically layered composites characterized by a hyperelastic constitutive behavior under macroscopic compressive loading conditions along the lamination direction. The numerical results show that, in order to obtain reliable predictions of microscopic instability failure mechanisms related to debonding and contact phenomena, cohesive surface deformations must be appropriately accounted in the model adopting a finite strain continuum mechanics formulation, although the loading path involves negligible displacement jumps at the cohesive interface (theoretically zero). This is not crucial for undamaged or partially damaged cohesive interfaces, where significant tangential cohesive tractions can be transmitted. Specifically, the numerical outcomes highlighted that as the structural integrity decreases to less than 20%, the differences between the critical load factors obtained by means of the proposed exact formulation and the simplified ones become strongly noticeable. As a matter of fact, in the simplified formulations adopted in most cases in the literature, cohesive surface deformations can be incorporated only approximatively considering surface rotations (simplified formulation I), if not completely neglected (simplified formulation II). The obtained numerical results show a substantial underestimation of critical load factors (reaching values of about 60%), especially for the lowest values of matrix/reinforcement stiffness ratio and for the highest values of reinforcement volume fraction investigated.

In addition, a higher influence of the finite deformation contributions appearing at cohesive-contact interfaces was shown when the primary instability is characterized by a long wavelength rather than a short one. To delve deeper into this concept, when the primary instability has a long wavelength, the finite deformation contributions at cohesive-contact interfaces become particularly effective. In such cases, the deformations occurring at these interfaces are more extensive and, therefore, have a more substantial effect on the overall failure behavior of the material. This is because the cohesive-contact interfaces play a critical role in transmitting forces and maintaining the structural integrity of the composite. On the other hand, when the primary instability has a shorter wavelength, the deformations at cohesive-contact interfaces may be relatively limited in scale. In this situation, the impact of nonlinear finite deformation contributions appearing at the cohesive interfaces becomes less prominent compared to the larger-scale deformations occurring elsewhere in the material.

In summary, such numerical evidence suggests that especially in scenarios in which the composite materials feature imperfect interfaces and instability phenomena characterized by a wavelength longer than the unit cell size, understanding and accurately accounting for finite deformation contributions at cohesive-contact interfaces are essential.

As a future perspective, the proposed modeling approach can be also generalized in a dynamic context to analyze the influence of interfacial debonding on incremental wave propagation properties of finitely strained metamaterials characterized by a perfectly or locally periodic microstructure, taking into account the geometry transformation induced by microscopic instabilities.

Fundings

Fabrizio Greco gratefully acknowledges financial support from the Italian Ministry of Education, University and Research (MIUR) under the P.R.I.N. 2022 National Grant "Innovative tensegrity lattices and architectured metamaterials (ILAM)" (Project Code 20224LBXMZ; University of Calabria Research Unit). Andrea Pranno gratefully acknowledges financial support from the POR Calabria FESR-FSE 2014-2020, Rep. N. 1006 of 30/03/2018, Line B, Action 10.5.12

References

1. Zhang Q, Cherkasov AV, Arora N, Hu G, Rudykh S. 2023 Magnetic field-induced asymmetric mechanical metamaterials. *Extreme Mechanics Letters* **59**, 101957. (doi:10.1016/j.eml.2023.101957)

2. Pranno A, Greco F, Leonetti L, Lonetti P, Luciano R, De Maio U. 2022 Band gap tuning through microscopic instabilities of compressively loaded lightened nacre-like composite metamaterials. *Composite Structures* **282**, 115032. (doi:10.1016/j.compstruct.2021.115032)

3. Jandyal A, Chaturvedi I, Wazir I, Raina A, Ul Haq MI. 2022 3D printing – A review of processes, materials and applications in industry 4.0. *Sustainable Operations and Computers* **3**, 33–42. (doi:10.1016/j.susoc.2021.09.004)

4. Siddique SH, Hazell PJ, Wang H, Escobedo JP, Ameri AAH. 2022 Lessons from nature: 3D printed bio-inspired porous structures for impact energy absorption – A review. *Additive Manufacturing* **58**, 103051. (doi:10.1016/j.addma.2022.103051)

5. De Maio U, Greco F, Luciano R, Sgambitterra G, Pranno A. 2023 Microstructural design for elastic wave attenuation in 3D printed nacre-like bioinspired metamaterials lightened with hollow platelets. *Mechanics Research Communications* **128**, 104045. (doi:10.1016/j.mechrescom.2023.104045)

6. Burlon A, Failla G. 2023 On the band gap formation in locally-resonant metamaterial thin-walled beams. *European Journal of Mechanics - A/Solids* **97**, 104798. (doi:10.1016/j.euromechsol.2022.104798)

7. Russillo AF, Failla G, Amendola A, Luciano R. 2022 On the Free Vibrations of Non-Classically Damped Locally Resonant Metamaterial Plates. *Nanomaterials* **12**, 541. (doi:10.3390/nano12030541)

8. Michel JC, Lopez-Pamies O, Ponte Castañeda P, Triantafyllidis N. 2010 Microscopic and macroscopic instabilities in finitely strained fiber-reinforced elastomers. *Journal of the Mechanics and Physics of Solids* **58**, 1776–1803. (doi:10.1016/j.jmps.2010.08.006)

9. Greco F, Lonetti P, Luciano R, Nevone Blasi P, Pranno A. 2018 Nonlinear effects in fracture induced failure of compressively loaded fiber reinforced composites. *Composite Structures* **189**, 688–699. (doi:10.1016/j.compstruct.2018.01.014)

10. Greco F, Leonetti L, Lonetti P, Luciano R, Pranno A. 2020 A multiscale analysis of instability-induced failure mechanisms in fiber-reinforced composite structures via alternative modeling approaches. *Composite Structures* **251**, 112529. (doi:10.1016/j.compstruct.2020.112529)

11. Triantafyllidis N, Maker BN. 1985 On the Comparison Between Microscopic and Macroscopic Instability Mechanisms in a Class of Fiber-Reinforced Composites. *Journal of Applied Mechanics* **52**, 794–800. (doi:10.1115/1.3169148)

12. Cricrì G, Luciano R. 2013 Homogenised properties of composite materials in large deformations. *Composite Structures* **103**, 9–17. (doi:10.1016/j.compstruct.2013.03.015)

13. Geymonat G, Muller S, Triantafyllidis N. 1993 Homogenization of nonlinearly elastic materials, microscopic bifurcation and macroscopic loss of rank-one convexity. *Arch. Rational Mech. Anal.* **122**, 231–290. (doi:10.1007/BF00380256)

14. Galich PI, Fang NX, Boyce MC, Rudykh S. 2017 Elastic wave propagation in finitely deformed layered materials. *Journal of the Mechanics and Physics of Solids* **98**, 390–410. (doi:10.1016/j.jmps.2016.10.002)

15. Galich PI, Slesarenko V, Rudykh S. 2017 Shear wave propagation in finitely deformed 3D fiber-reinforced composites. *International Journal of Solids and Structures* **110–111**, 294–304. (doi:10.1016/j.ijsolstr.2016.12.007)

16. Nezamabadi S, Yvonnet J, Zahrouni H, Potier-Ferry M. 2009 A multilevel computational strategy for handling microscopic and macroscopic instabilities. *Computer Methods in Applied Mechanics and Engineering* **198**, 2099–2110. (doi:10.1016/j.cma.2009.02.026)

17. Nezamabadi S, Potier-Ferry M, Zahrouni H, Yvonnet J. 2015 Compressive failure of composites: A computational homogenization approach. *Composite Structures* **127**, 60–68. (doi:10.1016/j.compstruct.2015.02.042)

18. Bigoni D, Ortiz M, Needleman A. 1997 Effect of interfacial compliance on bifurcation of a layer bonded to a substrate. *International Journal of Solids and Structures* **34**, 4305–4326. (doi:10.1016/S0020-7683(97)00025-5)

19. Lignon E, Le Tallec P, Triantafyllidis N. 2013 Onset of failure in a fiber reinforced elastomer under constrained bending. *International Journal of Solids and Structures* **50**, 279–287. (doi:10.1016/j.ijsolstr.2012.07.022)

20. Allix O, Corigliano A. 1999 Geometrical and interfacial non-linearities in the analysis of delamination in composites. *International Journal of Solids and Structures* **36**, 2189–2216. (doi:10.1016/S0020-7683(98)00079-1)

21. Tvergaard V. 1990 Effect of fibre debonding in a whisker-reinforced metal. *Materials Science and Engineering: A* **125**, 203–213. (doi:10.1016/0921-5093(90)90170-8)

22. Ortiz M, Pandolfi A. 1999 Finite-deformation irreversible cohesive elements for three-dimensional crack-propagation analysis. *Int. J. Numer. Meth. Engng.* **44**, 1267–1282. (doi:10.1002/(SICI)1097-0207(19990330)44:9<1267::AID-NME486>3.0.CO;2-7)

23. Xu Q, Lu Z. 2013 An elastic–plastic cohesive zone model for metal–ceramic interfaces at finite deformations. *International Journal of Plasticity* **41**, 147–164. (doi:10.1016/j.ijplas.2012.09.008)

24. Greco F, Leonetti L, Medaglia CM, Penna R, Pranno A. 2018 Nonlinear compressive failure analysis of biaxially loaded fiber reinforced materials. *Composites Part B: Engineering* **147**, 240–251. (doi:10.1016/j.compositesb.2018.04.006)

25. Greco F. 2013 A study of stability and bifurcation in micro-cracked periodic elastic composites including self-contact. *International Journal of Solids and Structures* **50**, 1646–1663. (doi:10.1016/j.ijsolstr.2013.01.036)

26. Bilbie G, Dascalu C, Chambon R, Caillerie D. 2008 Micro-fracture instabilities in granular solids. *Acta Geotechnica* **3**, 25–35. (doi:10.1007/s11440-007-0046-8)